Nanoscale Advances

ROYAL SOCIETY OF CHEMISTRY

COMMUNICATION

View Article Online
View Journal | View Issue

Cite this: *Nanoscale Adv.*, 2021, **3**, 4659

Received 26th May 2021
Accepted 23rd June 2021

DOI: 10.1039/d1na00389e

rsc.li/nanoscale-advances

Evidence of oxygen bubbles forming nanotube embryos in porous anodic oxides

Tianle Gong,† Chengyuan Li,† Xin Li, Hangyu Yue, Xufei Zhu, * Ziyu Zhao, Renquan Lv and Junwu Zhu *

Anodic TiO_2 nanotubes have been studied widely for two decades because of their regular tubular structures and extensive applications. However, the formation mechanism of anodic TiO_2 nanotubes remains unclear, because it is difficult to find convincing evidence for popular field-assisted dissolution or field-assisted injection theories and the oxygen bubble model. Here, in a bid to find direct evidence that oxygen bubbles form nanotube embryos, a new method is applied to handle this challenge. Before nanotube formation, a dense cover layer was formed to make nanotubes grow more slowly. Many completely enclosed nanotube embryos formed by oxygen bubbles were found beneath the dense cover layer for the first time. The formation of these enclosed and hollow gourd-shaped embryos is convincing enough to prove that the nanotubes are formed by the oxygen bubble mold, similar to inflating a football, rather than by field-assisted dissolution. Based on the 'oxygen bubble model' and ionic current and electronic current theories, the formation and growth process of nanotube embryos is explained clearly for the first time. These interesting findings indicate that the 'oxygen bubble model' and ionic current and electronic current theories also apply to anodization of other metals.

1. Introduction

Porous anodic oxides (TiO_2, Al_2O_3, Fe_2O_3, Ta_2O_5, *etc.*) have attracted much attention because of their unique nanoscale ordered structure and wide application.[1–8] Although porous anodic alumina and anodic TiO_2 nanotubes have been studied for decades, the formation mechanism of these porous nanoscale structures remains controversial.[1,9–15] First of all, is there any connection or difference between the porous structure and the nanotube structure? There is a main difference in the porous structure of porous anodic alumina and anodic TiO_2 nanotubes. The nanotube structure is created by oxide formation and dissolution due to the presence of fluoride ions.[15] As a result, a TiF_4 layer instead of a TiO_2 layer forms at the metal/oxide interface.[15] The solubility of the cell walls in anodizing electrolyte is the key factor that decides whether the oxide nanotube structure or porous structure is formed.[15] Therefore, the fluoride ions and water play a crucial role in the formation of nanotubes or porous structure.[15] But Huang *et al.*[16] obtained both the nanotube structure and the porous structure of TiO_2 by anodizing in the exact same NH_4F electrolyte.[16]

Secondly, the formation mechanisms of popular porous anodic oxides are all developed from the field-assisted dissolution theory of porous anodic alumina. For example, the field-assisted reaction of porous anodic alumina is $Al_2O_3 + 6H^+ \rightarrow 2Al^{3+} + 3H_2O$.[9,10] The field-assisted reaction of TiO_2 nanotubes is $TiO_2 + 6F^- + 4H^+ \rightarrow [TiF_6]^{2-} + 2H_2O$.[12,15,17] The field-assisted reaction of Ta_2O_5 nanotubes is $Ta_2O_5 + 10H^+ + 14F^- \rightarrow 2[TaF_7]^{2-} + 5H_2O$.[18] The field-assisted reaction of Fe_2O_3 nanotubes is $Fe_2O_3 + 12F^- + 6H^+ \rightarrow 2[FeF_6]^{3-} + 3H_2O$.[19] Although these reactions have been repeatedly cited to explain the mechanism of nanopore formation, it has never been reported that any of these dissolution reactions actually exist.[9–12,20] On the contrary, in recent years there have been a number of articles denying the field-assisted dissolution reaction.[20–23] Skeldon *et al.*[21] demonstrated that the acid dissolves alumina weakly,[21] which could not sustain the growth of the pores. Many researchers also demonstrated that the dissolution of titanium oxide by the fluoride ion is also weak.[22–25] Why is the formation mechanism of porous anodic oxides still controversial until now? We believe that the main reason is that the relationship between the above field-assisted dissolution reactions and anodizing current has not been clearly understood.[26–29] Why does the growth rate of nanotubes increase with the increase of anodizing current in the electrolyte with the same concentration of the fluoride ion?[30] The relationship between the field-assisted dissolution reaction of the fluoride ion and the total anodizing current has not been explained until now.[30–32] Thompson *et al.*[9] clearly pointed out that the above field-

Key Laboratory of Soft Chemistry and Functional Materials of Education Ministry, Nanjing University of Science and Technology, Nanjing 210094, China. E-mail: zhuxufei.njust@vip.163.com; zhujw@njust.edu.cn

† Authors Tianle Gong and Chengyuan Li contributed equally to this work.

assisted dissolution reaction is a pure chemical reaction, independent of the applied electric field.[9] In summary, the limitation of the above field-assisted dissolution reaction is that the physical meaning of electric field is not clear. How the electric field acts on the above dissolution reaction to assist the growth of nanotubes is also vague.[1,10–15,33–35]

The third controversy is about the two modes in which nanotubes grow, whether they grow in the "top-down digging mode" on the surface of the oxide film or in the "bottom-up flow mode" around the oxygen bubble under the oxide film.[1,10–12] It is well known that the three traditional theories of field-assisted dissolution, field-induced injection, oxide growth and dissolution equilibrium suggest that the growth of nanopores is in accordance with the "top-down digging mode".[33–42] However, the oxide viscous flow model and the 'oxygen bubble model' suggest that nanopores grow from the bottom to the top.[26,43,44] The ionic current causes the barrier oxide layer to grow upward around the oxygen bubble mold, creating the nanotube walls.[45–50]

Garcia-Vergara *et al.*[43] concluded that the viscous flow model and field-assisted dissolution theories are completely opposite in the way of the pore or nanotube formation.[43] However, there is little direct evidence on whether nanotube embryos are formed by field-assisted dissolution or by the 'oxygen bubble model'. Herein, a new approach was used to study the formation mechanism of nanotubes in order to identify whether the nanotubes originated from field-assisted dissolution or the oxide flow around the oxygen bubble mold. The substrate is firstly anodized in fluoride-free electrolyte to obtain a preformed dense cover layer. The second layer is anodized in fluoride-containing electrolyte to form the nanotubes. In this way, the preformed dense cover layer can work as a barrier to the infiltration of the electrolyte, which could eliminate the influence of field-assisted dissolution. Also, it is hard for the oxygen bubbles to be released from the film surface. The preformed dense cover layer makes it easier to see the structure of TiO_2 nanotube embryos from the FESEM images. It can work as direct evidence to verify the 'oxygen bubble model'. Porous or nanotube embryos are also found in anodization of Al and Zr. Based on ionic current and electronic current theories, the formation of porous or nanotube embryos is given a new explanation.

2. Experimental details

The experiment is divided into four parts. The details are presented as follows.

2.1. Part 1: the normal anodization process of Ti (no TiO_2 nanotube embryos)

Titanium foil (100 μm thick, purity 99.5%) was cut into 1.0 cm × 6.0 cm pieces. Before anodization, they were polished with a mixed solution of HF, HNO_3 and deionized water (1 : 1 : 2 by volume) for 15 s. The samples were then rinsed thoroughly with deionized water and dried in air. The titanium foil was the anode and a graphite plate served as the cathode. The anodization area was kept at 1.0 cm × 2.0 cm × 2 sides. The titanium foil was anodized in ethylene glycol electrolyte containing 0.5 wt% NH_4F, 2 wt% H_2O and 2 wt% H_3PO_4 at constant 50 V. The anodizing times were 30 s, 60 s and 500 s. In Part 1, there were no TiO_2 nanotube embryos seen. Only anodic TiO_2 nanotubes could be seen from the FESEM images.

2.2. Part 2: the two-step anodization process of Ti (the dense cover layer and TiO_2 nanotube embryos)

The cutting and polishing process is the same as that in Part 1. During the anodization, the titanium foil was the anode and a graphite plate served as the cathode. The anodization area was kept at 1.0 cm × 2.0 cm × 2 sides.

The first step of anodization was conducted in ethylene glycol electrolyte containing 5 wt% H_3PO_4 at 60 V for 300 s in order to form the dense cover layer. The second step of anodization was conducted in ethylene glycol electrolyte containing 0.5 wt% NH_4F, 2 wt% H_2O and 2 wt% H_3PO_4 at 70 V for 200 s and 300 s to form the TiO_2 nanotube embryos under the dense cover layer.

2.3. Part 3: the two-step anodization process of Al (the dense cover layer and porous anodic alumina embryos)

The aluminum sheets (0.2 mm thick, purity 99.99%) were cut into 1.0 cm × 6.0 cm pieces. Then, the aluminum sheets were dipped into aqueous solution containing 6 wt% H_3PO_4 at 40 °C for 30 minutes for polishing. After that, the samples were rinsed thoroughly with deionized water and dried in air. The aluminum sheet served as the anode and a graphite plate was employed as the cathode. The anodization area was kept at 1.0 cm × 2.0 cm × 2 sides. The first step of anodization was conducted in aqueous solution containing 10 wt% ammonium hypophosphite at constant 40 V for 300 s to form the dense cover layer. The second step of anodization was then conducted in aqueous solution containing 6 wt% H_3PO_4 at 70 V for 200 s and 300 s to form the porous anodic alumina embryos under the dense cover layer.

2.4. Part 4: the normal anodization process of Zr (ZrO_2 nanotube embryos)

Zirconium foil (100 μm thick, purity 99.5%) was cut into 1.0 cm × 6.0 cm pieces. Before anodization, they were polished with a mixed solution of HF, HNO_3 and deionized water (1 : 1 : 2 by volume) for 5 s. The samples were then rinsed thoroughly with deionized water and dried in air. The zirconium foil was the anode and a graphite plate served as the cathode. The anodization area was kept at 1.0 cm × 2.0 cm × 2 sides. The zirconium foil was anodized in ethylene glycol electrolyte containing 0.5 wt% NH_4F, 2 wt% H_2O and 2 wt% H_3PO_4 at constant 30 V for 600 s. As a result of the special structure of ZrO_2 nanotubes, ZrO_2 nanotube embryos were also seen in Part 4.

2.5. Extra details of part 1, 2, 3 and 4

The anodizing temperature was maintained at 15 °C *via* water bath cooling. The current–time curves of all the samples were

recorded using a computer system. After anodization, all the samples (Ti, Al, Zr) were firstly soaked in plenty of deionized water for an hour. Then they were rinsed using deionized water and dried in air to remove the solute remaining on the surface of the oxide film. Finally, to see the cross-sections of the oxide film on the substrate, the samples were bent into a Ω shape. A lot of cracks were caused to observe the nanotube embryos clearly. All the samples were characterized by FESEM (Zeiss Supra 55).

3. Results and discussion

3.1 The normal anodization process of Ti (no TiO_2 nanotube embryos)

Fig. 1a–c, show the FESEM images of the anodic oxide film of Ti anodized for 30 s, 60 s and 500 s. Fig. 1d shows the corresponding current–time curve (500 s) in Part 1. When Ti was anodized for 30 s, no TiO_2 nanotube embryos could be seen from the images and there were some little holes on the surface of the oxide film (Fig. 1a). However, when the anodizing time reached 60 s, the cross section of nanopores can be seen clearly (Fig. 1b). At the same time, the corresponding pits of nanopores are left on the Ti substrate (Fig. 1b). Fig. 1c shows a clear picture of the nanotubes anodized for 500 s. The pits on the Ti substrate at the bottom of the nanotubes are clearly visible. From the FESEM images of Fig. 1, it is hard to directly decide if the anodic TiO_2 nanotubes originated from the field-assisted dissolution or the 'oxygen bubble model'.

The curve of Fig. 1d displays three typical stages as reported.[23,30,47] Herein, we give the explanation of three stages based on field-assisted dissolution theory and the oxygen bubble model, respectively. According to the "top-down digging mode" of the field-assisted dissolution theory,[1] oxide is grown at both the electrolyte/oxide interface and the Ti/oxide interface in the stage (I) in Fig. 1d. Both interfaces grow oxides at the same time, so the thickness of the oxide film increases rapidly. Therefore, the total anodizing current also decreases rapidly to the lowest point and enters stage (II).[51–53] In stage (II), the field-assisted dissolution reaction leads to digging into nanotube embryos. The overall thickness of the oxide film becomes thin at the dissolved site (the surface hole on the oxide film in Fig. 1a and b). As a result, the anodizing current increased again in stage (II). In stage (III), after the formation of the nanotube embryos, the electrolyte enters the bottom of the nanotubes. The oxide growth at the bottom of the nanotubes occurs only at the Ti/oxide interface. At the electrolyte/oxide interface, only the field-assisted reaction occurs at the bottom of the nanotube, causing the pores to grow downward in the "top-down digging mode".

There are many limitations of field-assisted dissolution theory in explaining the formation process of nanotubes. For example, in stage (I), the oxide growth occurs at both interfaces. However, in stage (III), the growth of oxide only occurs at the Ti/oxide interface. Also, the oxide film formed in stage (I) is a complete whole (Fig. 1a). According to the "top-down digging mode" of field-assisted dissolution theory, it is impossible to form independent nanotubes in Fig. 1c. The gap between nanotubes cannot be explained according to field-assisted dissolution theory.[34] Also, the field-assisted dissolution reaction was denied by the flow model of the porous anodic film.[51] It has been confirmed that equilibrium between oxide growth and dissolution is impossible.[10,19]

However, based on ionic current and electronic current theories[31,52,54–58] and the 'oxygen bubble model',[24,59–62] the three typical stages in Fig. 1d can be given a clear explanation.

The following formulas can be defined:[27,29,54]

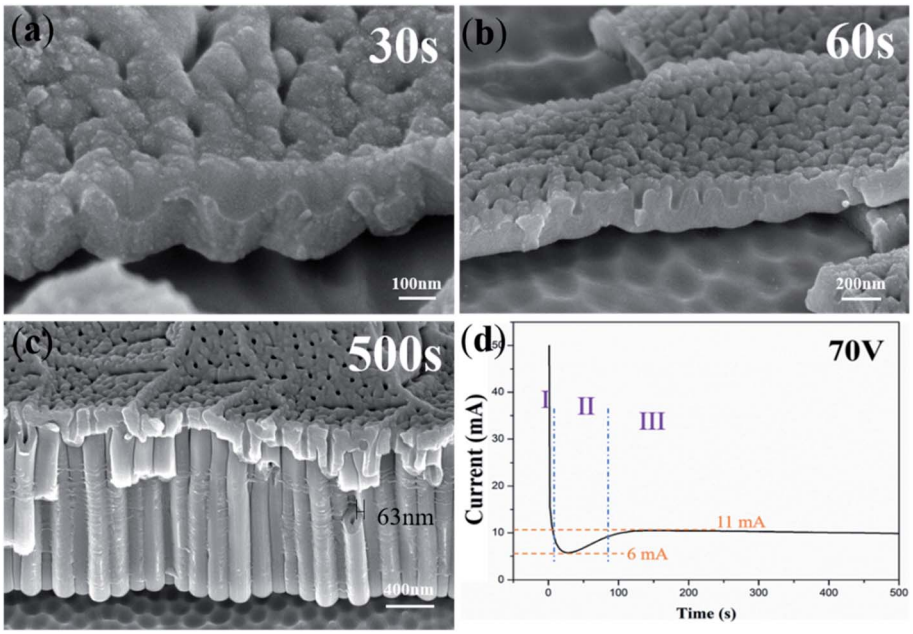

Fig. 1 FESEM images of anodic TiO_2 nanotubes anodized for (a) 30 s; (b) 60 s; (c) 500 s and (d) the corresponding current–time curve.

$$J_{ion} = A \exp(\beta E) = A \exp(\beta U/d) \quad (1)$$

$$J_e = J_0 \exp(\alpha d) \quad (2)$$

$$J_{total} = J_e + J_{ion} \quad (3)$$

In these three formulas, J_{ion} is the ionic current, J_e is the electronic current, J_{total} is the total current during the anodization, and J_0 is the primary electronic current.[54] α is the impact ionization coefficient of the avalanche. β and A are temperature dependent constants. E is the electric field strength, U is the applied voltage and d is the thickness of the barrier oxide layer. From the above formula, it can be seen that the electronic current decreases with the increase of oxide thickness. During the anodization process, it is surprising that the electronic current does increase with increase of oxide thickness.

In stage (I), the oxide film is formed rapidly with J_{total} decreasing dramatically. The driving force of the oxide growth is the ionic current. The new oxide grows at both the metal/oxide interface and the electrolyte/oxide interface.[20] At this stage, J_{total} is almost equal to the ionic current. The oxide film which is near the electrolyte will become an anion contaminated layer and the one which is near the Ti substrate will become a barrier oxide layer.[27,29,54] The ionic current decreases and the thickness of the barrier oxide layer becomes larger; according to $J_e = J_0 \exp(\alpha d)$, the magnitude of the electronic current becomes larger. When the barrier oxide layer reaches the critical thickness so as to the large amounts of electronic current generation. Then the process entered the stage (II). Therefore, stage (I) in Fig. 1d is dominated by the ionic current, and the lowest current (6 mA) is the ionic current in the subsequent anodization process.

In stage (II), J_{total} starts to climb because of the increase of the electronic current and oxygen bubbles start to release between the interface of the anion contaminated layer and the barrier oxide layer.[16,63] Under the pressure of the anion contaminated layer and the electrolyte, oxygen bubbles are not able to release from the surface at once. Thus, oxygen bubbles serve as a mold. The viscous flow of oxide grows around oxygen bubbles, leading to the formation of TiO_2 nanotube embryos. An appropriate ionic current is used to form new oxide around the growing oxygen bubbles and the sufficient electronic current causes the expansion of oxygen bubbles. Eventually, oxygen bubbles break through the overlying anion contaminated layer and evolve from the surface.[16,63] In stage (II), the increasing current is the electronic current (about 5 mA).

In stage (III), oxygen bubbles evolve from the bottom of the nanotubes and the electrolyte reaches the bottom of the nanotube. The ionic current and the electronic current are determined by the thickness of the barrier oxide layer. As a result of the constant thickness of the barrier oxide layer at the bottom of the nanotubes, the ionic current and the electronic current remain stable, at 6 mA and 5 mA in stage (III), respectively. The constant ionic current maintains oxide growth and the constant electronic current maintains oxygen evolution. The newly grown oxide promotes the upward growth of the tube wall in a viscous flow pattern around the oxygen bubble mold at the bottom of the nanotube.

3.2 TiO_2 nanotube embryos obtained under the preformed dense cover layer

In order to verify that the formation of nanotube embryos is not directly related to the surface dissolution reaction of fluorine ions, we designed two-step anodic oxidation experiments (Part 2). In the first step, the substrate is firstly anodized in fluoride-free electrolyte to obtain a preformed dense cover layer. The second layer is anodized in fluoride-containing electrolyte to form the nanotubes. As a result, we find countless nanotube embryos formed by oxygen bubbles under the complete dense cover layer.

Fig. 2a shows the FESEM images of the dense cover layer. In the fluoride-free electrolyte, there is hardly any electronic current, so only the dense film without holes can be formed. Thus, the dense cover layer can work as a barrier to the invasion of the electrolyte. Fig. 2b shows the TiO_2 nanotube embryos, which are formed in the second anodization, under the warped dense cover layer. The warping of the dense cover layer is caused by artificial bending in order to see the TiO_2 nanotube embryos more clearly. It can be speculated that there are TiO_2 nanotube embryos under the unwarped dense cover layer. According to field-assisted dissolution theory, the formation of anodic TiO_2 nanotubes is a result of the field-assisted dissolution of the oxide.[12] Obviously, the experimental results take the opposite position: with the preformed dense cover layer, it is impossible for the electrolyte containing fluoride ions to dig, thus forming the TiO_2 nanotube embryos. This result therefore puts field-assisted dissolution theory into question.

According to ionic current and electronic current theories,[31,52,54–58] the formation of anodic TiO_2 nanotubes is a result of the oxide flow around the oxygen bubble. Zhou *et al.*[20] suggested that when the growth of oxide exceeded the rate of the evolution of oxygen bubbles, the viscous flow of oxide around the oxygen bubbles led to the formation of the nanotube embryos.[20] Experiencing a short time of anodization, oxygen bubbles which grow between the interface of the barrier oxide layer and the anion contaminated layer have not yet evolved from the surface. Therefore, TiO_2 nanotube embryos, which are shaped like a bottle gourd, are formed according to the 'oxygen bubble model'.

Fig. 3 shows the FESEM images of TiO_2 nanotube embryos. Fig. 3a shows TiO_2 nanotube embryos under the surface of the dense cover layer. There is no pore on the surface of the dense cover layer, but the nanotube embryos can be seen from the big cracks. Originally a complete dense cover layer covered the top of the nanotube embryo. In order to see the TiO_2 nanotube embryos below the dense cover layer, the samples were subjected to artificial destruction during the FESEM sample preparation. The microstructures of TiO_2 nanotube embryos viewed from the side in Fig. 3b show that the TiO_2 nanotube embryos under the dense cover layer are almost all sealed, which means that it is hard for the electrolyte to dig into them to cause field-assisted dissolution. The morphology of the warped dense cover layer in Fig. 3c is similar to that in Fig. 2a. It can be reckoned that there are TiO_2 nanotube embryos under the unwarped

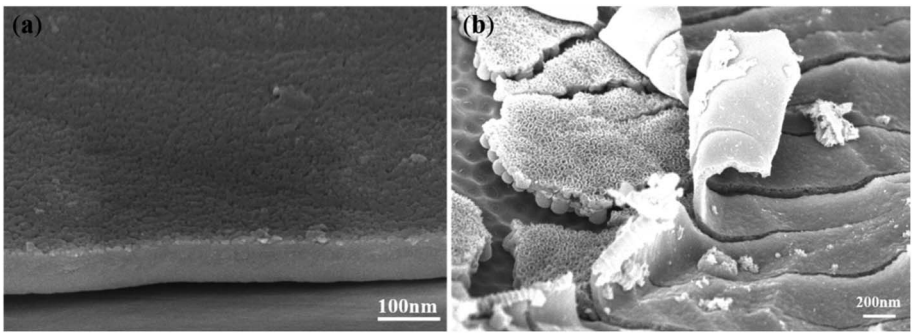

Fig. 2 FESEM images of (a) the TiO_2 dense cover layer formed by the first anodization; (b) the TiO_2 nanotube embryos under the artificial warped dense cover layer.

dense cover layer, which field-assisted dissolution theory cannot explain.

Fig. 3d is a local magnification diagram of sealed nanotube embryos in Fig. 3c. Fig. 3d shows that most of the TiO_2 nanotube embryos are sealed. That is to say, no corrosive electrolyte enters these sealed TiO_2 nanotube embryos and field-assisted dissolution cannot occur within the TiO_2 nanotube embryos. Therefore, these TiO_2 nanotube embryos are not formed by the field-assisted dissolution. We propose that the oxide flow around the oxygen bubbles forms the TiO_2 nanotube embryos.[24,60] The 'oxygen bubble model' suggests that the electronic current leads to the expansion of oxygen bubbles and TiO_2 nanotube embryos are formed with the growth of the oxide flow around oxygen bubbles in the "bottom-up flow mode". These hollow sealed TiO_2 nanotube embryos are seen more clearly in Fig. 4.

Fig. 4 shows the FESEM images of TiO_2 nanotube embryos and cavities in the dense cover layer. There was a clear spherical bottom morphology of the TiO_2 nanotube embryos as seen in Fig. 4a, which significantly deviates from the expectation of field-assisted dissolution theory. The dissolution of the electrolyte should be random and the bottom morphology of TiO_2 nanotube embryos cannot be the same. Also, the hemispherical pits on the substrate of Ti after artificial warping of TiO_2 nanotube embryos in Fig. 4b also puts the field-assisted dissolution theory into question. The "top-down digging mode" of dissolution cannot form the hemispherical pits on the substrate of Ti. Fig. 4c shows that the inside of the TiO_2 nanotube embryos is hollow. These facts indicate that the formation of gourd-shaped TiO_2 nanotube embryos results from the oxide flow around the oxygen bubbles.[24,60]

Also, Fig. 4c shows that the growth rate of nanotube embryos in the same sample is different. There are clear nanotube embryos on the left of Fig. 4c. However, cavities formed by oxygen bubbles can be seen on the right of Fig. 4c. These cavities are formed by the expansion of oxygen bubbles. Fig. 4d shows the cavities which have not formed the gourd-shaped nanotube embryos in the dense cover layer in the same sample. There is no crack on the surface of the dense cover layer. However, some cavities are observed in the dense cover layer in

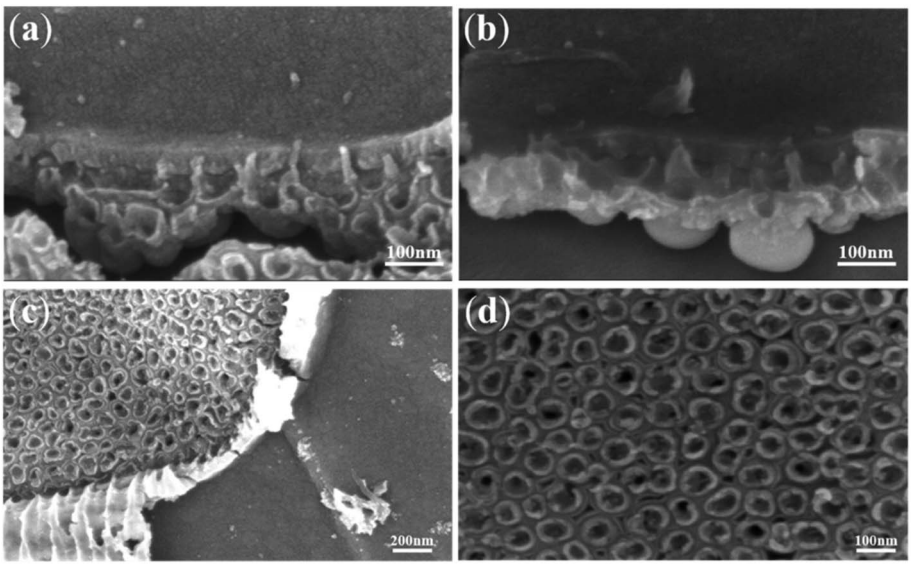

Fig. 3 FESEM images of TiO_2 nanotube embryos under the artificial warped dense cover layer.

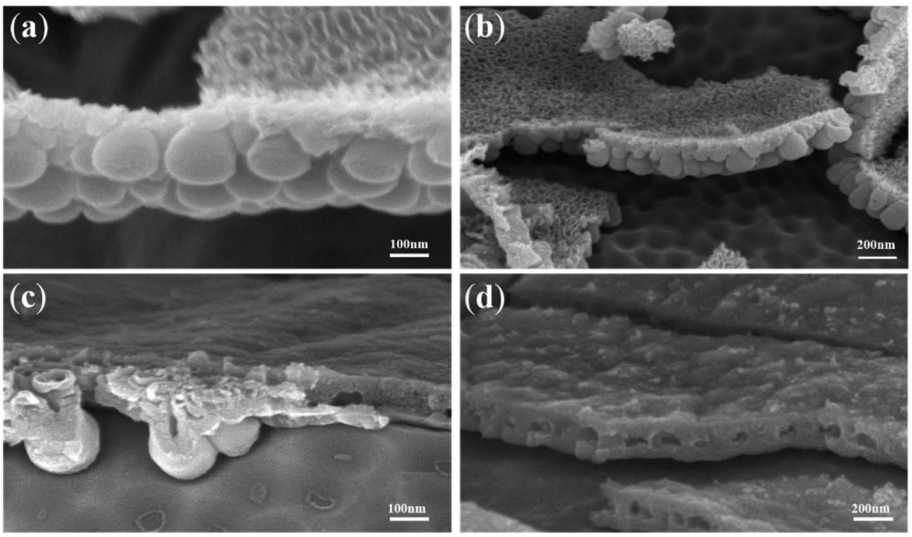

Fig. 4 FESEM images of the coexistence of the dense cover layer and gourd-shaped TiO_2 nanotube embryos.

Fig. 4d. These cavities, hidden in the dense cover layer, are obviously not the result of the "top-down digging mode" of the field-assisted dissolution. According to the 'oxygen bubble model' and ionic current and electronic current theories, the barrier oxide layer grows to the critical thickness and the electronic current causes the oxygen evolution.

3.3 Porous anodic alumina embryos obtained under the preformed dense cover layer

Interestingly, porous anodic alumina embryos are also found in the anodization of Al. Similar to the anodization of Ti, the anodization of Al is also conducted twice. The dense cover layer is formed during the first anodization, so the dense cover layer can work as a barrier to the invasion of the electrolyte. Fig. 5a shows porous anodic alumina embryos and the surface of the dense cover layer. There is no crack on the surface of the dense cover layer. According to field-assisted dissolution theory, the embryos are the result of the dissolution of the electrolyte.[1] However, the porous anodic alumina embryos under the dense cover layer significantly deviate from the expectation of field-assisted dissolution theory. Also, field-assisted dissolution theory cannot explain the protrusion of the surface in Fig. 5b. The dissolution of the electrolyte can only cause the digging of the dense cover layer, so the protrusion of the surface cannot be formed by field-assisted dissolution.

The warped dense cover layer in Fig. 5c is caused by artificial bending in the process of sample preparation. Similar to the result of embryos in Fig. 3c, without the dissolution of the electrolyte, it can be concluded that the formation of the porous anodic alumina embryos under the artificial warped dense

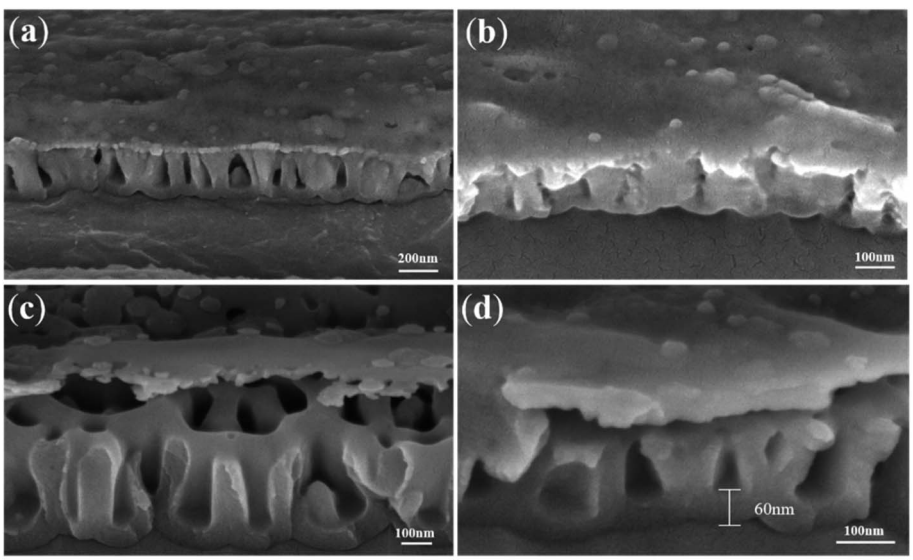

Fig. 5 FESEM images of porous anodic alumina embryos under the artificial warped dense cover layer.

cover layer in Fig. 5c is not the result of the field-assisted dissolution. According to ionic current and electronic current theories, the formation of porous anodic alumina is a result of the oxide flow around the oxygen bubble. Experiencing a short time of anodization, oxygen bubbles which grow between the interface of the barrier oxide layer and the anion contaminated layer have not yet evolved from the surface. Therefore, porous anodic alumina embryos are formed according to the 'oxygen bubble model'. The formation of cavities in Fig. 5d is the result of the expansion of oxygen bubbles. It indicates that the cavities are obviously not a result of the "top-down digging mode" of the field-assisted dissolution theory. Also, we believe that the difference between the porous structure (Fig. 5) and the nanotube structure (Fig. 1c) results from the electronic current. The electronic current in the anodization of Al is larger than that of Ti in the same phosphoric acid electrolyte.[64] The expansion of oxygen bubbles in the porous anodic alumina causes the disappearance of the gap between nanotubes, thus forming the porous anodic alumina.

3.4 ZrO_2 nanotube embryos obtained during the normal anodization process

A similar result is obtained during the anodization of Zr. As a result of the disordered arrangement of anodic ZrO_2 nanotubes, the anodization of Zr is conducted once. Fig. 6 shows the FESEM images of disordered ZrO_2 nanotube embryos and the corresponding current–time curve. Fig. 6a shows that the anodizing current decreases in stage (III), which is completely different from stage (III) in the current–time curve of the Ti anodization in Fig. 1d. The decrease of the anodizing current in Fig. 6a indicates that the dissolution equilibrium does not occur in the anodization of Zr, and therefore cannot form nanotubes according to field-assisted dissolution theory. However, Fig. 6b shows that both the columnar anodic ZrO_2 nanotubes and nanotube embryos are formed during the Zr anodization. It indicates that when the current in stage (III) is unstable, nanotubes can also be formed. This fact put field-assisted dissolution theory into question. As a result, the formation of nanotubes is not associated with the growth of oxide and the dissolution equilibrium, but depends on the existence of the electronic current and the ionic current. There are nanotube embryos on the left of Fig. 6b. However, long nanotubes can be seen on the right of Fig. 6b. It indicates that the growth rate of nanotubes in the same sample is different.

Fig. 7 shows different shapes of more ZrO_2 nanotube embryos in the same sample. There are some ZrO_2 nanotube embryos of different lengths as seen in Fig. 7a. Fig. 7b shows some sealed spherical ZrO_2 nanotube embryos. In Fig. 7c, open ZrO_2 nanotube embryos can be seen. Fig. 7d shows the local oxide film at the bottom of the nanotube embryos. By comparing the current–time curve in Fig. 1d and 6a, it can be concluded that in stage (III) in Fig. 1d, both the ionic current (6 mA) and electronic current (5 mA) are at a constant value. As a result, the oxides and oxygen bubbles at the bottom of the nanotubes grow together. The oxide at the bottom of the nanotubes can keep growing around the oxygen bubbles at the bottom of the nanotubes *via* the viscous flow pattern. Therefore, continuous vertical ordered nanotube arrays are obtained as shown in Fig. 1c. That is to say, when nanotubes grow, the ionic current and the electronic current are indispensable. The sufficient ionic current ensures tight oxide growth around oxygen bubbles. The adequate electronic current forms the sufficient volume of oxygen bubbles to serve as a mold. In this way, the outer diameter and inner diameter of nanotubes can remain unchanged. After the increase of the electronic current in stage (II), the oxygen bubbles are formed, thus leading to the formation of ZrO_2 nanotube embryos. However, the anodizing current after stage (II) decreases rapidly, which indicates that the ionic current and the electronic current are unstable. According to ionic current and electronic current theories, the anodizing curve rises when the electronic current increases and drops when the ionic current increases. The lowest point of turning is the magnitude of the ionic current and the highest point is the magnitude of electronic current. When more oxygen bubbles are formed, the number of ZrO_2 nanotube embryos will be larger. However, as a result of the discontinuous formation of oxygen bubbles, the nanotube embryos are shaped differently (globular and oval). Both the ionic current and the electronic

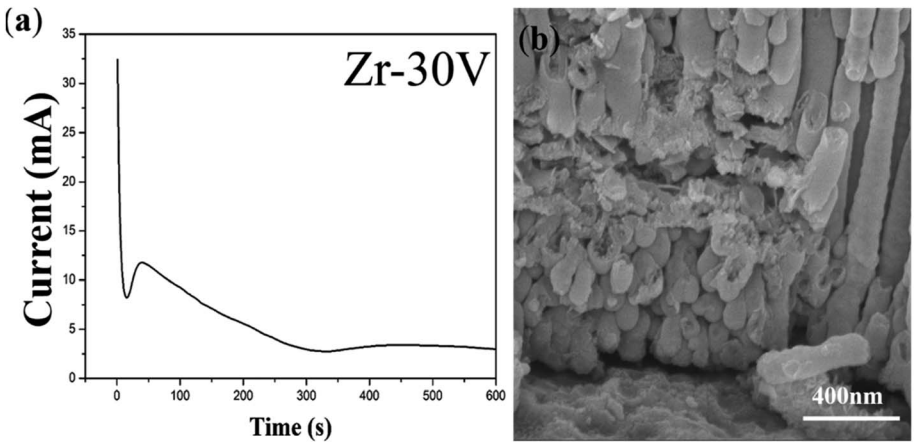

Fig. 6 (a) The current–time curve of the anodization process of Zr; (b) FESEM images of ZrO_2 nanotube embryos.

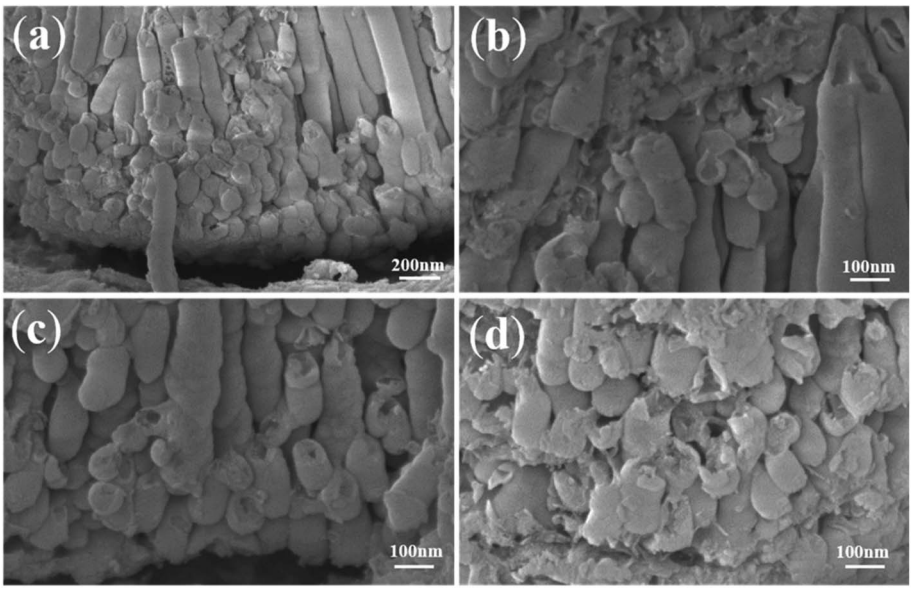

Fig. 7 FESEM images of anodic ZrO_2 (a) nanotube embryos and long nanotubes; (b) columnar nanotubes; (c) (d) the disordered arrangement of nanotube embryos.

current are in a downward trend, resulting in these ZrO_2 nanotube embryos failing to form complete nanotubes with a certain length.

4. Conclusions

Combinatorial anodization is exploited to monitor the nanotube formation process of Ti and Al under a preformed dense cover layer. With the dense cover layer, it is difficult for the electrolyte to penetrate. The experimental results show just the opposite of field-assisted dissolution theory. In the anodization of Ti, there are a lot of gourd-shaped TiO_2 nanotube embryos seen under the artificial warped dense cover layer. The formation of these gourd-shaped TiO_2 nanotube embryos is the result of the electronic current, which forms oxygen bubbles between the interface of the barrier oxide layer and the anion contaminated layer. Also, the growth rate of the nanotube embryos in the same sample is different. In the anodization of Al, some porous anodic alumina embryos under the artificial warped dense cover layer are seen. It indicates that the formation of porous anodic alumina embryos is also the result of the electronic current and oxygen bubbles. Also, we believe that there is little difference in the essence of the porous structure and the nanotube structure. Both of them result from the expansion of oxygen bubbles.

Nanotube embryos are also seen in the one-time anodization of Zr. According to field-assisted dissolution theory, the dissolution equilibrium in the third stage (III) forms nanotubes. However, during the process of the anodization of Zr, the anodizing current decreases in stage (III) and nanotube embryos of different lengths are formed. According to the 'oxygen bubble model', the decrease of the anodizing current in stage (III) indicates that the ionic current and the electronic current are unstable. As a result, the nanotube embryos are shaped differently. These interesting results presented in this paper are helpful to understand the growth mechanism of porous anodic oxides.

Author contributions

Tianle Gong: methodology, and writing – original draft. Chengyuan Li: methodology, writing – review & editing, and formal analysis. Xin Li: writing – review & editing, and investigation. Hangyu Yue: formal analysis, and validation. Xufei Zhu: conceptualization, and project administration. Ziyu Zhao: formal analysis. Renquan Lv: investigation. Junwu Zhu: supervision.

Conflicts of interest

There are no conflicts to declare.

Acknowledgements

This work was financially supported by the National Natural Science Foundation of China (Grant Nos. 51777097 and 51577093) and the National Undergraduate Training Program for Innovation and Entrepreneurship (202110288034Z).

References

1 A. Ruiz-Clavijo, O. Caballero-Calero and M. Martín-González, *Nanoscale*, 2021, **13**, 2227–2265.
2 Z. Q. Tong, S. K. Liu, X. G. Li, J. P. Zhao and Y. Li, *Nanoscale Horiz.*, 2018, **3**, 261–292.
3 C. P. Yu, Z. L. Zheng, W. C. Zhang, B. Hu, Y. J. Chen, J. H. Chen, K. F. Ma, J. H. Ye and J. W. Zhu, *ACS Sustainable Chem. Eng.*, 2020, **8**, 3969–3975.

4 Y. L. Wang, R. Jin, N. Sojic, D. C. Jiang and H. Y. Chen, *Angew. Chem., Int. Ed.*, 2020, **59**, 10416–10420.
5 S. Y. Cao, D. L. Yu, Y. Lin, C. Zhang, L. F. Lu, M. Yin, X. Zhu, X. Y. Chen and D. Li, *ACS Appl. Mater. Interfaces*, 2020, **12**, 26184–26192.
6 Z. Y. Yuan, S. W. Zhang, F. L. Meng, H. Zhang and K. Y. Zuo, *IEEE Sens. J.*, 2020, **20**, 4275–4282.
7 X. H. Xia, Z. Y. Zeng, X. L. Li, Y. Q. Zhang, J. P. Tu, N. C. Fan, H. Zhang and H. J. Fan, *Nanoscale*, 2013, **5**, 6040–6047.
8 X. Chen, X. R. Xu, J. Cui, C. T. Chen, X. Zhu, D. P. Sun and J. S. Qian, *J. Hazard. Mater.*, 2020, **392**, 122331.
9 J. Oh and C. V. Thompson, *Electrochim. Acta*, 2011, **56**, 4044–4051.
10 S. X. Liu, J. L. Tian and W. Zhang, *Nanotechnology*, 2021, **32**, 222001.
11 K. Y. Wang, G. H. Liu, N. Hoivik, E. Johannessen and H. Jakobsen, *Chem. Soc. Rev.*, 2014, **43**, 1476–1500.
12 R. Q. Hang, F. L. Zhao, X. H. Yao, B. Tang and P. K. Chu, *Appl. Surf. Sci.*, 2020, **517**, 146118.
13 H. Tsuchiya and P. Schmuki, *Nanoscale*, 2020, **12**, 8119–8132.
14 K. R. Hebert, S. Albu, I. Paramasivam and P. Schmuki, *Nat. Mater.*, 2012, **11**, 162–166.
15 F. Riboni, N. T. Nguyen, S. So and P. Schmuki, *Nanoscale Horiz.*, 2016, **1**, 445–466.
16 W. Q. Huang, H. Q. Xu, Z. R. Ying, Y. X. Dan, Q. Zhou, J. Zhang and X. F. Zhu, *Electrochem. Commun.*, 2019, **106**, 106532.
17 D. S. Guan and Y. Wang, *Nanoscale*, 2012, **4**, 2968–2977.
18 H. A. El-Sayed, C. A. Horwood, A. D. Abhayawardhana and V. I. Birss, *Nanoscale*, 2013, **5**, 1494–1498.
19 Y. D. Xue and Y. T. Wang, *Nanoscale*, 2020, **12**, 10912–10932.
20 Q. Y. Zhou, M. M. Tian, Z. R. Ying, Y. X. Dan, F. R. Tang, J. P. Zhang, J. W. Zhu and X. F. Zhu, *Electrochem. Commun.*, 2020, **111**, 106663.
21 O. O. Capraz, P. Shrotriya, P. Skeldon, G. E. Thompson and K. R. Hebert, *Electrochim. Acta*, 2015, **167**, 404–411.
22 Y. Zhang, W. Cheng, F. Du, S. Y. Zhang, W. Ma, D. Li, Y. Song and X. F. Zhu, *Electrochim. Acta*, 2015, **180**, 147–154.
23 H. Lu, H. Fan, R. Jin, B. Chong, X. Shen, S. Yan and X. F. Zhu, *Electrochim. Acta*, 2016, **215**, 380–387.
24 Z. Y. Zhang, Q. Wang, H. Q. Xu, W. C. Zhang, Q. Y. Zhou, H. P. Zeng, J. L. Yang, J. W. Zhu and X. F. Zhu, *Electrochem. Commun.*, 2020, **114**, 106717.
25 Z. Y. Zhang, Q. Q. Liu, M. F. He, F. R. Tang, Z. R. Ying, H. Q. Xu, Y. Song, J. W. Zhu and X. F. Zhu, *J. Electrochem. Soc.*, 2020, **167**, 113501.
26 J. E. Houser and K. R. Hebert, *Nat. Mater.*, 2009, **8**, 415–420.
27 X. F. Zhu, Y. Song, L. Liu, C. Y. Wang, J. Zheng, H. Jia and X. Wang, *Nanotechnology*, 2009, **20**, 475303.
28 Y. Li, Z. Y. Ling, X. Hu, Y. Liu and Y. Chang, *RSC Adv.*, 2012, **2**, 5164–5171.
29 X. F. Zhu, Y. Song, D. Yu, C. Zhang and W. Yao, *Electrochem. Commun.*, 2013, **29**, 71–74.
30 B. Chong, D. Yu, R. Jin, Y. Wang, D. Li, Y. Song, M. Gao and X. Zhu, *Nanotechnology*, 2015, **26**, 145603.
31 S. W. Zhao, J. Xing, H. W. Fan, S. Y. Zhang, D. Li and X. F. Zhu, *J. Electrochem. Soc.*, 2017, **164**, E187–E193.
32 S. W. Zhao, L. Z. Wu, C. Li, C. Y. Li, M. S. Yu, H. Cui and X. Zhu, *Electrochem. Commun.*, 2018, **93**, 25–30.
33 G. Patermarakis and K. Moussoutzanis, *Electrochim. Acta*, 2009, **54**, 2434–2443.
34 Z. X. Su and W. Z. Zhou, *J. Mater. Chem.*, 2011, **21**, 8955–8970.
35 P. Roy, S. Berger and P. Schmuki, *Angew. Chem., Int. Ed.*, 2011, **50**, 2904–2939.
36 W. Lee and S. J. Park, *Chem. Rev.*, 2014, **114**, 7487–7556.
37 D. Regonini, C. R. Bowen, A. Jaroenworaluck and R. Stevens, *Mater. Sci. Eng. R Rep.*, 2013, **74**, 377–406.
38 H. Masuda and K. Fukuda, *Science*, 1995, **268**, 1466–1468.
39 G. D. Sulka, J. Kapusta-Kolodziej, A. Brzózka and M. Jaskula, *Electrochim. Acta*, 2013, **104**, 526–535.
40 J. M. Macak, M. Jarosova, A. Jäger, H. Sopha and M. Klementová, *Appl. Surf. Sci.*, 2016, **371**, 607–612.
41 A. M. Abd-Elnaiem, A. M. Mebed, W. J. Stępniowski and T. Czujko, *Surf. Coat. Technol.*, 2016, **307**, 359–365.
42 P. Parnicka, P. Mazierski, W. Lisowski, T. Klimczuk, J. Nadolna and A. Zaleska-Medynska, *Results Phys.*, 2019, **12**, 412–423.
43 S. J. Garcia-Vergara, P. Skeldon, G. E. Thompson and H. Habazaki, *Electrochim. Acta*, 2006, **52**, 681–687.
44 D. J. LeClere, A. Velota, P. Skeldon, G. E. Thompson, S. Berger, J. Kunze, P. Schmuki, H. Habazaki and S. Nagata, *J. Electrochem. Soc.*, 2008, **155**, C487–C494.
45 X. F. Zhu, L. Liu, Y. Song, H. B. Jia, H. D. Yu, X. M. Xiao and X. L. Yang, *Monatsh. Chem.*, 2008, **139**, 999–1003.
46 J. W. Cao, Z. Q. Gao, C. Wang, H. M. Muzammal, W. Q. Wang, Q. Gu, C. Dong, H. T. Ma and Y. P. Wang, *Surf. Coat. Technol.*, 2020, **388**, 125592.
47 S. Chen, Y. L. Ni, J. P. Zhang, Y. X. Dan, W. C. Zhang, Y. Song and X. F. Zhu, *Electrochem. Commun.*, 2021, **125**, 106991.
48 M. S. Yu, H. M. Cui, F. P. Ai, L. F. Jiang, J. Kong and X. F. Zhu, *Electrochem. Commun.*, 2018, **86**, 80–84.
49 K. Zhang, S. K. Cao, C. Li, J. R. Qi, L. F. Jiang, J. J. Zhang and X. F. Zhu, *Electrochem. Commun.*, 2019, **103**, 88–93.
50 J. J. Zhang, W. Q. Huang, K. Zhang, D. Z. Li, H. Q. Xu and X. F. Zhu, *Electrochem. Commun.*, 2019, **100**, 48–51.
51 G. E. Thompson, *Thin Solid Films*, 1997, **297**, 192–201.
52 D. Li, L. Zhao, C. H. Jiang and J. G. Lu, *Nano Lett.*, 2010, **10**, 2766–2771.
53 D. Kowalski, D. Kim and P. Schmuki, *Nano Today*, 2013, **8**, 235–264.
54 J. M. Albella, I. Montero and J. M. Martinez-Duart, *Electrochim. Acta*, 1987, **32**, 255–258.
55 A. Mazzarolo, M. Curioni, A. Vicenzo, P. Skeldon and G. E. Thompson, *Electrochim. Acta*, 2012, **75**, 288–295.
56 A. D. Pauric, S. A. Baig, A. Pantaleo, Y. Wang and P. Kruse, *J. Electrochem. Soc.*, 2013, **160**, C12–C18.
57 S. W. Zhao, T. Lu, H. M. Cui, D. L. Yu, S. Y. Zhang, J. S. Kong and X. F. Zhu, *J. Electrochem. Soc.*, 2017, **164**, E401–E407.
58 N. Lu, J. P. Zhang, Y. X. Dan, M. Sun, T. L. Gong, X. Li and X. F. Zhu, *Electrochem. Commun.*, 2021, **126**, 107022.

59 P. Y. Deng, X. D. Bai, X. W. Chen and Q. L. Feng, *J. Electrochem. Soc.*, 2004, **151**, B284–B289.
60 Q. Y. Zhou, D. M. Niu, X. J. Feng, A. C. Wang, Z. R. Ying, J. P. Zhang, N. Lu, J. W. Zhu and X. F. Zhu, *Electrochem. Commun.*, 2020, **119**, 106815.
61 J. W. Cao, C. Wang, Z. Q. Gao, S. Y. Shang, Q. D. Gu, N. Gao, Y. P. Wang and H. T. Ma, *ECS J. Solid State Sci. Technol.*, 2020, **9**, 104010.
62 L. Li, Z. X. Zhang, L. L. Bo, Y. J. Cui, Y. M. Xu and Z. F. Zhang, *Surf. Coat. Technol.*, 2020, **404**, 126470.
63 M. S. Yu, C. Li, Y. B. Yang, S. K. Xu, K. Zhang, H. M. Cui and X. F. Zhu, *Electrochem. Commun.*, 2018, **90**, 34–38.
64 M. S. Yu, H. M. Cui, H. Li, S. Y. Zhang, J. S. Kong, S. W. Zhao, F. P. Ai, Y. Song and X. F. Zhu, *J. Phys. Chem. C*, 2018, **122**, 549–556.